

Linearized Aw-Rascle-Zhang Model for Road Traffic Prediction and Control

Francois Belletti, Mandy Huo, Xavier Litrico, Alexandre M. Bayen

Abstract—This article starts from the classical Aw-Rascle-Zhang (ARZ) model for freeway traffic and develops a spectral analysis of its linearized version. A counterpart to the Froude number in hydrodynamics is defined that enables a classification of the nature of vehicle traffic flow using the explicit solution resulting from the analysis. We prove that our linearization about an equilibrium is stable for congested regimes and unstable otherwise. NGSIM data for congested traffic trajectories is used so as to confront the linearized model's predictions to actual macroscopic behavior of traffic. The model is shown to achieve good accuracy for speed and flow. In particular, it replicates the propagation of boundary conditions' oscillations into the interior resolution domain of the PDE under study.

I. INTRODUCTION

In traffic control and data mining communities, non-linearity most of the time presents challenges when it comes to devising control strategies or applying estimation theory. Empirical studies of goodness of fit would usually have researchers elect non-linear first order models such as LWR [CITE] or non-linear second order models such as [CITE]. [REPHRASE].

In that regard, second order models such as PW [CITE] were first presented as a compelling opportunity to account for many features empirically observed in traffic such as Although Daganzo highlighted many flaws of the first generation of that family of models, a second generation offered a step towards more realism in macroscopic traffic modeling. Talk about good properties of ARZ, a word about phase transition models. [REPHRASE]

Unfortunately, mathematical properties such as the inf-morphism principle [CITE CLAUDEL, BLANDIN, HOFTLEINER] have not found straightforward analogs in bi-variate second order models. The non-linearity of these models is therefore a strong challenge when it comes to devising control and data assimilation strategies with such models. [REPHRASE]

ARZ features phenomena of persisting linear oscillations that an accurate model for traffic is expected to account for. Similarly, traffic instability has been observed in practice and gave rise to many theoretical studies (Jamitons). Linearizing the ARZ model, based on the work of Litrico, offers a compelling opportunity to work in a realistic modeling framework where the phenomena mentioned above are present and, at the same time, use linear control theory and spectral Laplace analysis. [REPHRASE]

Our approach in this paper is therefore to linearize the ARZ model about an equilibrium so as to make the best of a trade-off between model accuracy and ease of use. The first section is dedicated to the linearization and spectral analysis of the ARZ model. We prove there is convective instability in free-flow regime that drives the model away from its equilibrium and devise an equivalent of the hydrodynamics' Froude number for traffic macroscopic models. Laplace transforms and low frequency analysis also present many properties whose interpretation is tractable and simple. The second section focuses on the accuracy of the model. It confronts its predictions with ground truth data extracted from the NGSIM data with [GIVE CHARACTERISTICS OF DATA SET]. It also shows how to leverage spectral analysis so as to compute traffic prediction without the need for finite difference or Riemann based numerical schemes. [REPHRASE]

II. THE ARZ MODEL

We consider the ARZ model with relaxation term. The model is shown here:

$$\rho_t + (\rho v)_x = 0, \quad (1)$$

$$(v - V(\rho))_t + v(v - V(\rho))_x = \frac{V(\rho) - v}{\tau}, \quad (2)$$

where ρ is the density, v is the velocity, τ is the relaxation time, and $V(\rho) = Q(\rho)/\rho$ is the equilibrium velocity profile, where $Q(\rho)$ is the density-flow relation given by the fundamental diagram. We assume that V is C^1 derivable over its domain. Without the relaxation term cars never reach the maximum allowable speed [?] and the steady-state relation between density and speed is broken in the presence of road junctions [?]. Note that at the equilibrium velocity this term is zero.

In vector form the ARZ model is

$$\begin{pmatrix} \rho \\ v \end{pmatrix}_t + C_1(\rho, v) \begin{pmatrix} \rho \\ v \end{pmatrix}_x = \begin{pmatrix} 0 \\ \frac{V(\rho) - v}{\tau} \end{pmatrix}. \quad (3)$$

where

$$C_1(\rho, v) = \begin{pmatrix} v & \rho \\ 0 & v + \rho V'(\rho) \end{pmatrix} \quad (4)$$

With the appropriate variable change, we can rewrite the model in the density-flow and velocity-flow forms, the latter of which is most useful to us for practical control purposes. Using the flow relation $q = \rho v$ and (6), the density-flow form is

$$\begin{pmatrix} \rho \\ q \end{pmatrix}_t + C_2(\rho, q) \begin{pmatrix} \rho \\ q \end{pmatrix}_x = \begin{pmatrix} 0 \\ \frac{Q(\rho)-q}{\tau} \end{pmatrix}. \quad (5)$$

$$\begin{pmatrix} v \\ q \end{pmatrix}_t + C_3(v, q) \begin{pmatrix} v \\ q \end{pmatrix}_x = \frac{1}{\tau} \left(V\left(\frac{q}{v}\right) - v \right). \quad (6)$$

where

$$C_2(\rho, q) = \begin{pmatrix} 0 & 1 \\ -\frac{q}{\rho} \left(\frac{q}{\rho} + \rho V'(\rho) \right) & 2\frac{q}{\rho} + \rho V'(\rho) \end{pmatrix} \quad (7)$$

$$C_3(v, q) = \begin{pmatrix} v + \frac{q}{v} V'\left(\frac{q}{v}\right) & 0 \\ \frac{q}{v} \left(v + \frac{q}{v} V'\left(\frac{q}{v}\right) \right) & v \end{pmatrix} \quad (8)$$

It is noteworthy that 5 is equivalent to the conservative form

$$\begin{pmatrix} \rho \\ q - Q(\rho) \end{pmatrix}_t + \begin{pmatrix} q \\ \rho(q - Q(\rho)) \end{pmatrix}_x = \begin{pmatrix} 0 \\ \frac{Q(\rho)-q}{\tau} \end{pmatrix} \quad (9)$$

most helpful in [?] and [?] for data assimilation and macroscopic traffic simulation respectively.

The (v, q) form has seldom been used in transportation engineering however it is promising for data fusion purposes that involve both loop detector measurements (providing values for q) and GPS traces (giving estimates for v).

A. Linearization

We are interested in small deviations, $(\tilde{\rho}(x, t), \tilde{v}(x, t))$, from a given nominal profile. Consider the nominal solution $(\rho^*(x), v^*(x))(V(\rho^*) = v^*)$ satisfying $v_t = \rho_t = 0$. Then (6) becomes

$$v^* \rho_x^* + v_x^* \rho^* = 0, \quad (10)$$

$$(v^* + \rho^* V'(\rho^*)) v_x^* = \frac{V(\rho^*) - v^*}{\tau} = 0. \quad (11)$$

Then we must have $v_x^* = \rho_x^* = 0$, so the solution is uniform along the road.

Linearizing the ARZ model (6) around the nominal solution described above, we obtain

$$\begin{pmatrix} \tilde{\rho} \\ \tilde{v} \end{pmatrix}_t + \bar{C}_1 \begin{pmatrix} \tilde{\rho} \\ \tilde{v} \end{pmatrix}_x = \bar{B}_1 \begin{pmatrix} \tilde{\rho} \\ \tilde{v} \end{pmatrix}. \quad (12)$$

$$(13)$$

where

$$\bar{C}_1 = \begin{pmatrix} v^* & \rho^* \\ 0 & v^* + \rho^* V'(\rho^*) \end{pmatrix} \quad (14)$$

$$\bar{B}_1 = -\frac{1}{\tau} \begin{pmatrix} 0 & 0 \\ V'(\rho^*) & -1 \end{pmatrix} \quad (15)$$

Similarly, for the density-flow system (5) we linearize around the equilibrium $(\rho^*, q^*)(\rho^* V'(\rho^*) = q^*)$ with deviations $(\tilde{\rho}(x, t), \tilde{q}(x, t))$. The analogs of \bar{C}_1 and \bar{B}_1 are denoted \bar{C}_2 and \bar{B}_2 in 16 and 18. For the

deviations (\tilde{v}, \tilde{q}) from the equilibrium we adopt similar notations with \bar{C}_3 and \bar{B}_3 given in 18 and 19. This last form, most adapted to traffic prediction and control in practical settings where flows and vehicle velocities are measured will be studied in what follows.

$$\bar{C}_2 = \begin{pmatrix} 0 & 1 \\ -\frac{q^*}{\rho^*} \left(\frac{q^*}{\rho^*} + \rho^* V'(\rho^*) \right) & 2\frac{q^*}{\rho^*} + \rho^* V'(\rho^*) \end{pmatrix} \quad (16)$$

$$\bar{B}_2 = \frac{1}{\tau} \begin{pmatrix} 0 & 0 \\ V'(\rho^*) & -1 \end{pmatrix} \quad (17)$$

$$\bar{C}_3 = \begin{pmatrix} v^* + \frac{q^*}{v^*} V'\left(\frac{q^*}{v^*}\right) & 0 \\ \frac{q^*}{v^*} \left(v^* + \frac{q^*}{v^*} V'\left(\frac{q^*}{v^*}\right) \right) & v^* \end{pmatrix} \quad (18)$$

$$\bar{B}_3 = \frac{1}{v^* \tau} \begin{pmatrix} -(v^*)^2 + q^* V'\left(\frac{q^*}{v^*}\right) & V'\left(\frac{q^*}{v^*}\right) \\ -\frac{v^*}{q^* \left((v^*)^2 + q^* V'\left(\frac{q^*}{v^*}\right) \right)} & \frac{q^* V'\left(\frac{q^*}{v^*}\right)}{(v^*)^2} \end{pmatrix} \quad (19)$$

$$(20)$$

B. Characteristic form

We diagonalize the linearized equations to obtain a more useful form of the model, which will then be treated in the spectral domain. We begin with the density-flow system. Standard algebraic manipulations of the equations in (12) lead to

$$\begin{pmatrix} \xi_1 \\ \xi_2 \end{pmatrix}_t + \begin{pmatrix} \lambda_1 & 0 \\ 0 & \lambda_2 \end{pmatrix} \begin{pmatrix} \xi_1 \\ \xi_2 \end{pmatrix}_x = \begin{pmatrix} -\frac{1}{\tau} & 0 \\ -\frac{1}{\tau} & 0 \end{pmatrix} \begin{pmatrix} \xi_1 \\ \xi_2 \end{pmatrix}, \quad (21)$$

where $\xi_1 = \tilde{v} - V'(\rho^*) \tilde{\rho}$ and $\xi_2 = \tilde{v}$ are the Riemann invariants of the (ρ, v) system, and $\lambda_1 = v^*$ and $\lambda_2 = v^* + \rho^* V'(\rho^*)$ are the eigenvalues. Note that $V'(\rho^*) \leq 0$ so $\lambda_2 \leq \lambda_1 = v^*$. Therefore this is consistent with the physical dynamics of the system as no waves travel faster than the equilibrium vehicle speed.

We proceed in the same manner as above to diagonalize the (ρ, q) system (??). The diagonal form is

$$\begin{pmatrix} \chi_1 \\ \chi_2 \end{pmatrix}_t + \begin{pmatrix} \lambda_1 & 0 \\ 0 & \lambda_2 \end{pmatrix} \begin{pmatrix} \chi_1 \\ \chi_2 \end{pmatrix}_x = \begin{pmatrix} -\frac{1}{\tau} & 0 \\ -\frac{1}{\tau} & 0 \end{pmatrix} \begin{pmatrix} \chi_1 \\ \chi_2 \end{pmatrix}, \quad (22)$$

where $\chi_1 = -\lambda_2 \tilde{\rho} + \tilde{q}$ and $\chi_2 = -\lambda_1 \tilde{\rho} + \tilde{q}$ are the characteristic variables in the (ρ, q) system and the eigenvalues λ_1 and λ_2 are the same as in the density-velocity system due to the relation $q^* = \rho^* v^*$.

Diagonalization of the velocity-flow system is more involved. Letting $\eta(x, t) = (\tilde{v}, \tilde{q})^T$, we can rewrite (??) as

$$\eta_t + A \eta_x = B \eta. \quad (23)$$

The eigenvalues of A are $\lambda_1 = v^*$ and $\lambda_2 = v^* + \frac{q^*}{v^*} V'\left(\frac{q^*}{v^*}\right)$, consistent with the previous systems.

Then A can be diagonalized as follows

$$A = XDX^{-1}, \quad (24)$$

$$X = \begin{pmatrix} 0 & \lambda_2 - \lambda_1 \\ 1 & \rho^* \lambda_2 \end{pmatrix}, \quad (25)$$

$$D = \begin{pmatrix} \lambda_1 & 0 \\ 0 & \lambda_2 \end{pmatrix}, \quad (26)$$

$$X^{-1} = \begin{pmatrix} \frac{\rho^* \lambda_2}{\lambda_1 - \lambda_2} & 1 \\ -\frac{1}{\lambda_1 - \lambda_2} & 0 \end{pmatrix}. \quad (27)$$

Define $\gamma(x, t) := X\eta(x, t)$. Hence (23) can be rewritten as

$$\gamma_t + \begin{pmatrix} \lambda_1 & 0 \\ 0 & \lambda_2 \end{pmatrix} \gamma_x = \begin{pmatrix} -\frac{1}{\tau} & 0 \\ -\frac{1}{q^* \tau} & 0 \end{pmatrix} \gamma \quad (28)$$

where

$$\gamma = \begin{pmatrix} \frac{\rho^* \lambda_2}{\lambda_1 - \lambda_2} \tilde{v} + \tilde{q} \\ -\frac{1}{\lambda_1 - \lambda_2} \tilde{v} \end{pmatrix}. \quad (29)$$

Let $\xi = (\xi_1, \xi_2)^T = (\chi_1, -q^* \chi_2)^T$. Then we have

$$\begin{pmatrix} \xi_1 \\ \xi_2 \end{pmatrix}_t + \underbrace{\begin{pmatrix} \lambda_1 & 0 \\ 0 & \lambda_2 \end{pmatrix}}_{\tilde{A}} \begin{pmatrix} \xi_1 \\ \xi_2 \end{pmatrix}_x = \underbrace{\begin{pmatrix} -\frac{1}{\tau} & 0 \\ -\frac{1}{\tau} & 0 \end{pmatrix}}_{\tilde{B}} \begin{pmatrix} \xi_1 \\ \xi_2 \end{pmatrix}, \quad (30)$$

and

$$\begin{pmatrix} \xi_1 \\ \xi_2 \end{pmatrix} = \begin{pmatrix} \frac{\rho^* \lambda_2}{\lambda_1 - \lambda_2} \tilde{v} + \tilde{q} \\ \frac{q^*}{\lambda_1 - \lambda_2} \tilde{v} \end{pmatrix} = \underbrace{\begin{pmatrix} \frac{\rho^* \lambda_2}{\lambda_1 - \lambda_2} & 1 \\ \frac{q^* \lambda_1}{\lambda_1 - \lambda_2} & 0 \end{pmatrix}}_R \begin{pmatrix} \tilde{v} \\ \tilde{q} \end{pmatrix} \quad (31)$$

C. The Traffic Froude Number

In fluid mechanics, the Froude number is a dimensionless number which delineates the boundary between flow regimes [?], [?]. Using the eigenvalues of the system in the characteristic form, we are able to define a useful counterpart to this number. Since $V(\rho)$ is non-increasing function, we have $V'(\rho^*) \leq 0$. Assuming $V'(\rho^*) \neq 0$ there are two flow regimes: one in which $\lambda_1 \lambda_2 < 0$ and one characteristic line travels downstream whereas the other characteristic line travels upstream, and one in which $\lambda_1 \lambda_2 > 0$ and both characteristic lines travel downstream.

We define the *Traffic Froude Number* (TFN) as

$$F = \left| \frac{\rho^* V'(\rho^*)}{v^*} \right|. \quad (32)$$

Then we have

$$\begin{cases} F > 1 \Rightarrow |\rho^* V'(\rho^*)| > v^* \Rightarrow \lambda_2 < 0 \\ F < 1 \Rightarrow |\rho^* V'(\rho^*)| < v^* \Rightarrow \lambda_2 > 0 \end{cases}.$$

Note also that $\lambda_2 = v^* + \rho^* V'(\rho^*) = \frac{Q(\rho^*)}{\rho^*} + \frac{\rho^* Q'(\rho^*) - Q(\rho^*)}{\rho^*} = Q'(\rho^*)$. Hence the system is in free-flow when $F < 1$ and congestion when $F > 1$.

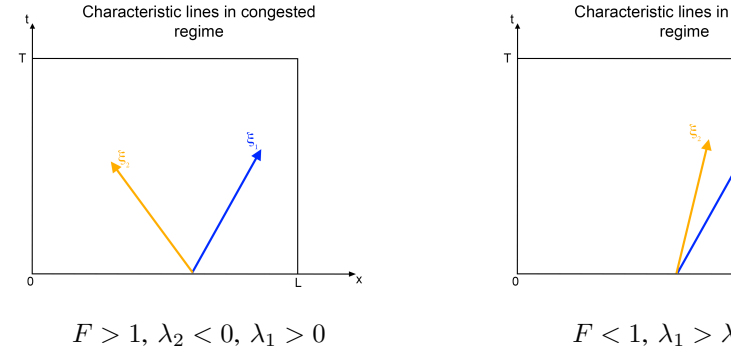


Fig. 1. Illustration of characteristic lines in congested (supercritical) and free-flow regime (subcritical) ξ_1 and ξ_2 propagate along.

In hydrodynamics these regimes are referred to as the subcritical and supercritical regimes, respectively [?]. The direction of characteristic lines is illustrated in Figure 1.

For traffic, the interpretation of the different regimes is somewhat different. Free flow regime corresponds to these situations where drivers are not slowed down by heavy traffic and go as fast as the desired speed. The congested regime arises when traffic is denser and, because too many cars are present on the same freeway section, drivers slow down and eventually form traffic jam.

III. SPECTRAL ANALYSIS OF THE LINEARIZED ARZ MODEL

We now consider the (v, q) system for the frequency domain analysis for practical control purposes.

A. State-transition matrix

Taking the Laplace transform of the diagonalized form (30) we obtain

$$\frac{d\hat{\xi}(x, s)}{dx} = \mathcal{A}(s)\hat{\xi}(x, s) + \mathcal{B}\xi(x, t=0^-), \quad (33)$$

where $\mathcal{A}(s) = \tilde{A}^{-1}(\tilde{B} - sI)$ and $\mathcal{B} = -\tilde{A}^{-1}$. The general solution to this ordinary differential equation is

$$\hat{\xi}(x, s) = \Phi(x, s)\hat{\xi}(0, s) + \Phi(x, s) \int_0^x \Phi(\nu, s)^{-1} \mathcal{B}\xi(\nu, 0^-) d\nu, \quad (34)$$

where $\Phi(x, s) = e^{\mathcal{A}(s)x}$ is the state-transition matrix. Assuming zero initial conditions we have

$$\hat{\xi}(x, s) = \Phi(x, s)\hat{\xi}(0, s). \quad (35)$$

To compute the exponential we diagonalize the matrix as

$$\mathcal{A}(s) = \mathcal{X}(s)\mathcal{D}(s)\mathcal{X}^{-1}(s) \quad (36)$$

where

$$\mathcal{X}(s) = \begin{pmatrix} 0 & \frac{\lambda_2 - (\lambda_1 - \lambda_2)\tau s}{\lambda_1} \\ 1 & 1 \end{pmatrix}, \quad (37)$$

$$\mathcal{D}(s) = \begin{pmatrix} -\frac{s}{\lambda_2} & 0 \\ 0 & -\frac{1+\tau s}{\tau \lambda_1} \end{pmatrix}. \quad (38)$$

Hence

$$\Phi(x, s) = \mathcal{X}^{-1}(s) e^{\mathcal{D}(s)x} \mathcal{X}(s) = \begin{pmatrix} \phi_{11}(x, s) & \phi_{12}(x, s) \\ \phi_{21}(x, s) & \phi_{22}(x, s) \end{pmatrix} \quad (39)$$

with

$$\phi_{11}(x, s) = e^{-\frac{x}{\tau\lambda_1}} e^{-\frac{x}{\lambda_1}s}, \quad (40a)$$

$$\phi_{12}(x, s) = 0, \quad (40b)$$

$$\phi_{21}(x, s) = \frac{\lambda_1 \left(e^{-\frac{x}{\tau\lambda_1}} e^{-\frac{x}{\lambda_1}s} - e^{-\frac{x}{\lambda_2}s} \right)}{\lambda_2 - \tau(\lambda_1 - \lambda_2)s}, \quad (40c)$$

$$\phi_{22}(x, s) = e^{-\frac{x}{\lambda_2}s}. \quad (40d)$$

Let $\alpha = -\frac{\lambda_2}{\tau(\lambda_1 - \lambda_2)}$. It is clear that $\phi_{11}(x, s)$ is composed of the product of a distributed delay corresponding to information propagating at speed λ_1 and an exponential attenuation where $\tau\lambda_1$ plays the role of a characteristic spatial length. Similarly ϕ_{22} is a delay corresponding to information propagating at speed λ_2 . The interpretation of ϕ_{21} is more difficult. In low frequencies ($|s| \ll |\alpha|$), this transfer function takes a much more transparent form. Indeed, in the expression $\phi_{21}(x, s) = -\frac{\lambda_1}{\lambda_2} \frac{\alpha}{s+\alpha} e^{-\frac{x}{\lambda_2}s} \left(1 - e^{-\frac{x}{\lambda_1\tau\alpha}(s+\alpha)} \right) \simeq -\frac{\lambda_1}{\lambda_2} e^{-\frac{x}{\lambda_2}s} \left(1 - e^{-\frac{x}{\lambda_1\tau}} \right)$ the transfer function appears as the combination of a distributed delay where λ_2 is the propagation speed and a distributed gain where $\lambda_1\tau$ is a characteristic distance.

B. Free-flow case ($F < 1$)

Consider the system in the free-flow regime.

With $\xi_1(0, t)$ and $\xi_2(0, t)$ as the inputs and $\xi_1(L, t)$ and $\xi_2(L, t)$ as the outputs, the distributed transfer matrix is exactly the state-transition matrix $\Phi(x, s)$.

Using (31), we can write

$$\begin{pmatrix} \tilde{v}(x, s) \\ \tilde{q}(x, s) \end{pmatrix} = \underbrace{\begin{pmatrix} \frac{\rho^*\lambda_2}{\lambda_1 - \lambda_2} & 1 \\ \frac{\rho^*\lambda_1}{\lambda_1 - \lambda_2} & 0 \end{pmatrix}}_{\Psi(x, s)}^{-1} \Phi(x, s) \begin{pmatrix} \frac{\rho^*\lambda_2}{\lambda_1 - \lambda_2} & 1 \\ \frac{\rho^*\lambda_1}{\lambda_1 - \lambda_2} & 0 \end{pmatrix} \quad (41)$$

with

$$\psi_{11}(x, s) = \frac{\alpha e^{-\frac{x}{\lambda_1}(s+\frac{1}{\tau})} + se^{-\frac{x}{\lambda_2}}}{s + \alpha}, \quad (42a)$$

$$\psi_{12}(x, s) = \frac{1}{\rho^*\tau} \frac{e^{-\frac{x}{\lambda_2}} - e^{-\frac{x}{\lambda_1}(s+\frac{1}{\tau})}}{s + \alpha}, \quad (42b)$$

$$\psi_{21}(x, s) = -s\rho^*\tau\alpha \frac{e^{-\frac{x}{\lambda_2}} - e^{-\frac{x}{\lambda_1}(s+\frac{1}{\tau})}}{s + \alpha}, \quad (42c)$$

$$\psi_{22}(x, s) = \frac{se^{-\frac{x}{\lambda_1}(s+\frac{1}{\tau})} + \alpha e^{-\frac{x}{\lambda_2}}}{s + \alpha}. \quad (42d)$$

It could appear at first sight that $-\alpha$ (here a positive real) is a singularity of the transfer functions and the system is not bounded-input/bounded-output stable.

However, we have $\frac{1}{\lambda_1}(-\alpha + \frac{1}{\tau}) = \frac{1}{\tau(\lambda_1 - \lambda_2)} = \frac{-\alpha}{\lambda_2}$, thus a Taylor expansion about $-\alpha$ shows that numerators and denominators cancel each other out for $s \rightarrow -\alpha$. It follows that $-\alpha$ is not a pole of any transfer function. This proves that the output remains bounded for a given value of x . We will show below that a conic region of the $[0, T] \times [0, L]$ domain features exponential growth in free-flow regime. This arises when changing t and x simultaneously and complements the conclusion formulated above (in which t varies and x remains constant).

1) Low frequency approximation for physical variables in free-flow regime: Analyzing the expressions above becomes easier when approximating them for $|s| \ll |\alpha|$. This corresponds to traffic flow varying slowly and smoothly. We find the following approximate expressions for the transfer functions:

$$\psi_{11}(x, s) = e^{-\frac{sx}{\lambda_2}} \frac{s + \alpha e^{-\frac{x}{\tau\lambda_1\alpha}(s+\alpha)}}{s + \alpha} \simeq e^{-\frac{sx}{\lambda_2}} e^{-\frac{x}{\tau\lambda_1\alpha}(s+\alpha)} \quad (43a)$$

$$\psi_{12}(x, s) = \frac{1}{\rho^*\tau} e^{-\frac{sx}{\lambda_2}} \frac{1 - e^{-\frac{x}{\tau\lambda_1\alpha}(s+\alpha)}}{s + \alpha} \simeq \frac{1}{\rho^*\tau\alpha} e^{-\frac{sx}{\lambda_2}} \left(1 - e^{-\frac{x}{\tau\lambda_1\alpha}(s+\alpha)} \right) \quad (43b)$$

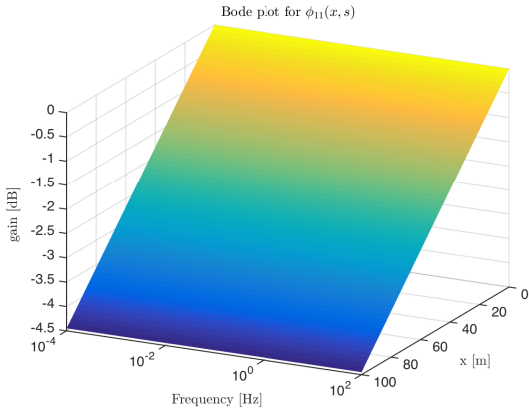
$$\psi_{21}(x, s) = -s\rho^*\tau\alpha e^{-\frac{sx}{\lambda_2}} \frac{1 - e^{-\frac{x}{\tau\lambda_1\alpha}(s+\alpha)}}{s + \alpha} \simeq -s\rho^*\tau\alpha e^{-\frac{sx}{\lambda_2}} \left(1 - e^{-\frac{x}{\tau\lambda_1\alpha}(s+\alpha)} \right) \quad (43c)$$

$$\psi_{22}(x, s) = e^{-\frac{sx}{\lambda_2}} \frac{\alpha + se^{-\frac{x}{\tau\lambda_1\alpha}(s+\alpha)}}{s + \alpha} \simeq e^{-\frac{sx}{\lambda_2}} \left(\alpha + se^{-\frac{x}{\tau\lambda_1\alpha}(s+\alpha)} \right) \quad (43d)$$

Interpreting the low frequency expressions is fairly straightforward:

- In ψ_{11} , $e^{-\frac{sx}{\lambda_2}}$ is a distributed delay with propagation speed λ_2 and $e^{-\frac{x}{\tau\lambda_1\alpha}}$ a distributed gain with characteristic distance $\tau\lambda_1$.
- In ψ_{12} and ψ_{21} we can notice the combination of a distributed delay whose characteristic speed is λ_2 and a distributed gain whose characteristic distance is $\tau\lambda_1$. It is also remarkable that $\tilde{q}(x, s)$ appears as the result of a derivator applied to $\tilde{v}(0, s)$.
- The approximate expression for ψ_{22} highlights the presence of a distributed delay where information propagates at speed λ_2 .

2) Bode plots for free-flow regime: We generate Bode plots using the following parameters taken from [?]: $q_{\max} = 1300$ veh/h, $\rho_{\max} = 0.1$ veh/m, and $L = 100$ m. The Greenshields fundamental diagram, $Q(\rho) = 4 \frac{q_{\max}}{\rho_{\max}^2} \rho(\rho_{\max} - \rho)$, is used to approximate the fundamental diagram. For inhomogeneous second-order models, the relaxation time, τ , falls in the range of about 14-60 seconds [?]. A relaxation time of $\tau = 15$ s is used for the following simulations. We simulate for $\rho^* = 0.01$ veh/m. Here the characteristic frequency of the system, $|\alpha|$, equals 0.53 Hz which is indeed sensible for traffic flow modeling.



Spatial magnitude Bode plot for $\phi_{11}(x, s)$.

Fig. 2. Spatial magnitude Bode plots for Riemann invariants in free-flow regime ($|\alpha| = 0.53$ Hz)

The Bode plots for the physical variables are displayed in Figure 3. For the Riemann invariants only $\phi_{21}(x, s)$ and $\phi_{22}(x, s)$ are represented in Figure 2 ($\phi_{11}(x, s)$ and $\phi_{12}(x, s)$ are only delay functions).

For transfer functions featuring $1 - e^{-\frac{x}{\lambda_1 \tau^\alpha}}(s+\alpha)$ as a factor (that is to say ϕ_{21} , ψ_{12} , and ψ_{21}) one can observe in the corresponding Bode plots that the value of the log-gain in high frequency tends to vary very sharply. Indeed, with $s = jw$, $\left|1 - e^{-\frac{x}{\lambda_1 \tau^\alpha}}(s+\alpha)\right| = e^{-\frac{x}{\lambda_1 \tau}} \sqrt{\left(e^{\frac{x}{\lambda_1 \tau}} - \cos\left(\frac{w}{\lambda_1 \tau^\alpha} x\right)\right)^2 + \sin^2\left(\frac{w}{\lambda_1 \tau^\alpha} x\right)}$.

Therefore, if the spatial pseudo-period $\tilde{L} = \frac{2\pi}{w} \lambda_1 \tau |\alpha|$ is low enough, near zero values appear when x is a multiple of \tilde{L} . This explains the irregular shape of the distributed Bode plots of ϕ_{21} , ψ_{12} , and ψ_{21} for frequencies $w \gg 2\pi \frac{\lambda_1 \tau |\alpha|}{\tilde{L}} = 6.53$ Hz. This does not impact the stability of the system. Bode plots only look irregular about such points because of the logarithmic scale.

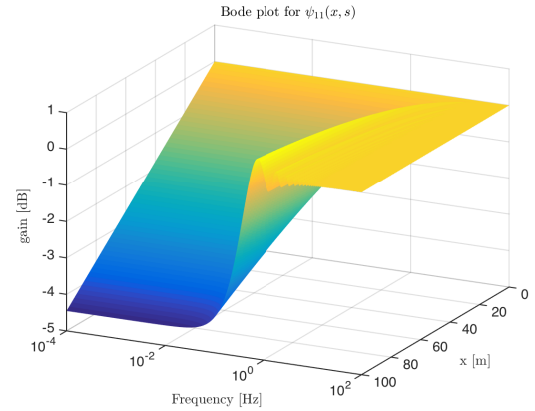
3) *Step responses*: We analyze the behavior of the system given step inputs $\tilde{v}(0, t) = v_{\text{step}}H(t)$ and $\tilde{q}(0, t) = q_{\text{step}}H(t)$, where $H(\cdot)$ is the Heaviside function. The step responses can be explicitly computed from the spectral responses:

$$\tilde{v}(x, t) = v_{\text{step}} \left[e^{-\frac{x}{\lambda_1 \tau}} H\left(t - \frac{x}{\lambda_1}\right) + e^{-\alpha\left(t - \frac{x}{\lambda_2}\right)} \left(H\left(t - \frac{x}{\lambda_2}\right) - H\left(t - \frac{x}{\lambda_1}\right) \right) \right] \\ - \frac{q_{\text{step}}}{\rho^* \tau} \left[e^{-\frac{x}{\lambda_1 \tau}} H\left(t - \frac{x}{\lambda_1}\right) - H\left(t - \frac{x}{\lambda_2}\right) + e^{\frac{C_\alpha}{\lambda_2} \text{Congested regime}} \left(H\left(t - \frac{x}{\lambda_2}\right) - H\left(t - \frac{x}{\lambda_1}\right) \right) \right].$$

(44) We now consider the

$$\begin{aligned} \tilde{q}(x, t) &= v_{\text{step}} \rho^* \tau \alpha e^{-\alpha(t - \frac{x}{\lambda_2})} \left(H\left(t - \frac{x}{\lambda_1}\right) - H\left(t - \frac{x}{\lambda_2}\right) \right) \quad \text{Using (35) we can write} \\ &+ q_{\text{step}} \left[H\left(t - \frac{x}{\lambda_2}\right) + e^{-\alpha(t - \frac{x}{\lambda_2})} \left(H\left(t - \frac{x}{\lambda} \begin{cases} \hat{\xi}_1(x, s) \\ \hat{\xi}_2(x, s) \end{cases} \right) \right) \right] \begin{pmatrix} 1 & 0 \\ -\frac{\phi_{21}(L, s)}{\phi_{22}(L, s)} & \frac{1}{\phi_{22}(L, s)} \end{pmatrix} \begin{pmatrix} \hat{\xi}_1(0, s) \\ \hat{\xi}_2(L, s) \end{pmatrix}. \end{aligned} \quad (45)$$

With this set of time domain expressions, we can see that a cone of exponentially growing speed and



Spatial magnitude of the Bode plot for $\phi_2(x)$.

The figure displays a 3D surface plot of the Bode magnitude for the system $\psi_{21}(x, s)$. The vertical axis represents the gain in dB, ranging from -150 to 0. The horizontal axis represents frequency in Hz on a logarithmic scale, with major ticks at 10^{-4} , 10^{-2} , 10^0 , 10^2 , and 10^4 . The depth axis represents position x in meters, with major ticks at 0, 20, 40, 60, and 80. The surface shows a sharp resonance peak near $x = 40$ m at approximately 10 Hz, with a maximum gain of about 10 dB. As frequency increases, the gain decreases, eventually leveling off around -10 dB at high frequencies.

Spatial magnitude Bode plot for $\psi_{21}(x, s)$.

Fig. 3. Spatial magnitude Bode plots for physical variables in free-flow regime ($|\alpha| = 0.53$ Hz)

flow linearization errors generally appears between the characteristic lines corresponding to λ_1 and λ_2 . This is caused by α being negative in the free flow regime and means that, in this region of the domain $[0, T] \times [0, L]$, the (v, q) state of the linearized system can diverge exponentially fast from the linearization point. This is consistent with the observations in [?] where small local perturbations occurring in free-flow regime can cause traffic to transition durably to the congested regime.

We now consider the system in the congested regime.

$$-\frac{x^2}{\lambda_2} \text{Using (35) we can write}$$

$$\underbrace{\frac{x}{\lambda} \begin{pmatrix} g_1(x, s) \\ g_2(x, s) \end{pmatrix} \left(t - \frac{x}{\Phi^2(x, s)} \right)}_{\Gamma(x, s)} \begin{pmatrix} 1 & 0 \\ -\frac{\phi_{21}(L, s)}{\phi_{22}(L, s)} & \frac{1}{\phi_{22}(L, s)} \end{pmatrix} \begin{pmatrix} \hat{\xi}_1(0, s) \\ \hat{\xi}_2(L, s) \end{pmatrix}. \quad (46)$$

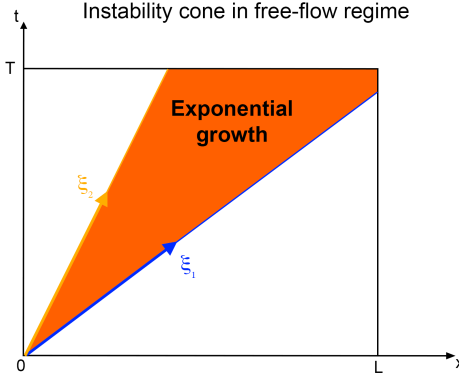


Fig. 4. Illustration of the exponential growth cone appearing in the free-flowing regime for the time domain expressions of v and q .

with

$$\gamma_{11}(x, s) = e^{-\frac{x}{\lambda_1}(s+\frac{1}{\tau})}, \quad (47a)$$

$$\gamma_{12}(x, s) = 0, \quad (47b)$$

$$\gamma_{21}(x, s) = \frac{\lambda_1}{\lambda_2} \frac{\alpha}{s + \alpha} e^{-\frac{x}{\lambda_1}(s+\frac{1}{\tau})} \left(1 - e^{-\frac{(L-x)}{\lambda_1 \tau \alpha}(s+\alpha)}\right), \quad (47c)$$

$$\gamma_{22}(x, s) = e^{\frac{s(L-x)}{\lambda_2}}. \quad (47d)$$

Note that equation (46) corresponds to a closed form solution of our initial system, written in spectral form.

For low frequencies ($|s| \ll |\alpha|$), $\gamma_{21}(x, s) \simeq \frac{\lambda_1}{\lambda_2} e^{-\frac{x}{\lambda_1}(s+\frac{1}{\tau})} \left(1 - e^{-\frac{L-x}{\lambda_1 \tau}}\right)$ is the combination of a gain, a distributed delay with propagation speed λ_1 , and two distributed gains with characteristic distance $\lambda_1 \tau$ that cancel out for $x = L$. The resulting bode plot is presented below in Figure 5.

1) *Transfer functions for physical variables in congested regime:* In congested regime, the boundary conditions used to control the system are $\hat{\xi}_1(0, \cdot)$ and $\hat{\xi}_2(0, \cdot)$. By linearity of the Laplace transform $\hat{\xi}_1(0, s) = \frac{\rho^* \lambda_2}{\lambda_1 - \lambda_2} \hat{v}(0, s) + \hat{q}(0, s)$. Therefore, as $\hat{\xi}_2(0, s) = \gamma_{21}(0, s) \hat{\xi}_1(0, s) + \gamma_{22}(0, s) \hat{\xi}_2(L, s)$, we get $\hat{\xi}_1(0, s) = \frac{1}{d(s)} \hat{q}(0, s) + \frac{n(s)}{d(s)} \hat{v}(L, s)$ where $d(s) = 1 - \frac{\lambda_2}{\lambda_1} \gamma_{21}(0, s)$ and $n(s) = \frac{\rho^* \lambda_2}{\lambda_1 - \lambda_2} \gamma_{22}(0, s)$. The (v, q) system has only two degrees of freedom. Therefore we consider that the only inputs to the system are $q(0, \cdot)$ and $v(L, \cdot)$. $v(0, \cdot)$ is then completely determined and can be interpreted as an output of the system. The corresponding transfer equation is

$$\begin{pmatrix} \hat{v}(x, s) \\ \hat{q}(x, s) \end{pmatrix} = \underbrace{R^{-1} \Gamma(x, s) \begin{pmatrix} \frac{n(s)}{d(s)} & \frac{1}{d(s)} \\ \frac{\rho^* \lambda_1}{\lambda_1 - \lambda_2} & 0 \end{pmatrix}}_{\Theta(x, s)} \begin{pmatrix} \hat{v}(L, s) \\ \hat{q}(0, s) \end{pmatrix} \quad (48)$$

where

$$\theta_{11}(x, s) = \frac{\alpha e^{-\frac{x}{\tau \lambda_1}} e^{-\frac{s}{\lambda_1} \left(x - L \frac{\lambda_1}{\lambda_2}\right)} + s e^{-\frac{s}{\lambda_2} (x-L)}}{s + \alpha e^{-\frac{L}{\tau \lambda_1}} e^{-\frac{sL}{\lambda_1} \left(1 - \frac{\lambda_1}{\lambda_2}\right)}}, \quad (49a)$$

$$\theta_{12}(x, s) = \frac{1}{\rho^* \tau} \frac{e^{-\frac{L}{\tau \lambda_1}} e^{-\frac{s}{\lambda_2} \left(x - L \left(1 - \frac{\lambda_2}{\lambda_1}\right)\right)} - e^{-\frac{x}{\tau \lambda_1}} e^{-\frac{s}{\lambda_1} (x-L)}}{s + \alpha e^{-\frac{L}{\tau \lambda_1}} e^{-\frac{sL}{\lambda_1} \left(1 - \frac{\lambda_1}{\lambda_2}\right)}}, \quad (49b)$$

$$\theta_{21}(x, s) = \rho^* \tau \alpha s \frac{e^{-\frac{s(x-L)}{\lambda_2}} - e^{-\frac{x}{\tau \lambda_1}} e^{-\frac{s}{\lambda_1} \left(x - L \frac{\lambda_1}{\lambda_2}\right)}}{s + \alpha e^{-\frac{L}{\tau \lambda_1}} e^{-\frac{sL}{\lambda_1} \left(1 - \frac{\lambda_1}{\lambda_2}\right)}}, \quad (49c)$$

$$\theta_{22}(x, s) = \frac{\alpha e^{-\frac{L}{\tau \lambda_1}} e^{-\frac{s}{\lambda_2} \left(x - L \left(1 - \frac{\lambda_2}{\lambda_1}\right)\right)} + s e^{-\frac{x}{\tau \lambda_1}} e^{-\frac{s}{\lambda_1} (x-L)}}{s + \alpha e^{-\frac{L}{\tau \lambda_1}} e^{-\frac{sL}{\lambda_1} \left(1 - \frac{\lambda_1}{\lambda_2}\right)}}. \quad (49d)$$

2) *Low frequency approximation for physical variables in congested regime:* We derive approximate expressions in the frequency domain for the transfer functions above when $|s| \ll |\alpha|$:

$$\theta_{11}(x, s) = \frac{e^{\frac{s(L-x)}{\lambda_2}} \left(s + \alpha e^{-\frac{x}{\tau \lambda_1 \alpha} (s+\alpha)}\right)}{s + \alpha e^{-\frac{L}{\tau \lambda_1 \alpha} (s+\alpha)}} \quad (50a)$$

$$\theta_{12}(x, s) = \frac{1}{\rho^* \tau} e^{-\frac{x}{\lambda_1} \left(s + \frac{1}{\tau}\right)} \frac{e^{-\frac{(L-x)}{\tau \lambda_1 \alpha} (s+\alpha)} - 1}{s + \alpha e^{-\frac{L}{\tau \lambda_1 \alpha} (s+\alpha)}} \simeq \frac{1}{\rho^* \tau \alpha} e^{-\frac{s x}{\lambda_1}} \quad (50b)$$

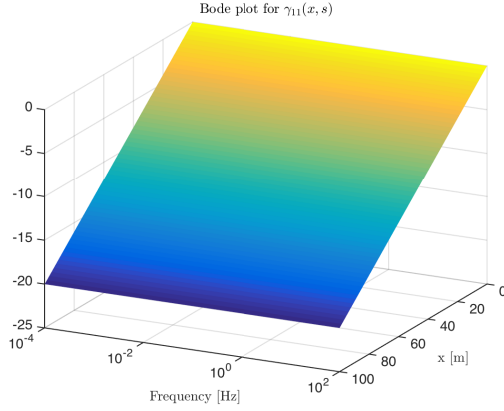
$$\theta_{21}(x, s) = s \rho^* \tau \alpha e^{\frac{s(L-x)}{\lambda_2}} \frac{1 - e^{-\frac{x}{\tau \lambda_1 \alpha} (s+\alpha)}}{s + \alpha e^{-\frac{L}{\tau \lambda_1 \alpha} (s+\alpha)}} \simeq s \rho^* \tau e^{\frac{s(L-x)}{\lambda_2}} e^{\frac{L}{\tau \lambda_1}} \quad (50c)$$

$$\theta_{22}(x, s) = e^{-\frac{x}{\lambda_1} \left(s + \frac{1}{\tau}\right)} \frac{\alpha e^{-\frac{(L-x)}{\tau \lambda_1 \alpha} (s+\alpha)} + s}{s + \alpha e^{-\frac{L}{\tau \lambda_1 \alpha} (s+\alpha)}} \quad (50d)$$

With such expressions, interpreting the approximate transfer functions in low frequencies becomes fairly easy:

- The transfer function θ_{11} (resp. θ_{12}) appears as the combination of a distributed delay with propagation speed $-\lambda_2$ (resp. λ_1) and a distributed gain (resp. attenuation) with characteristic distance $\lambda_1 \tau$.
- The structure of θ_{21} is similar to that of θ_{11} although it features a derivator component.
- Once simplified, θ_{22} corresponds to a distributed delay with propagation speed λ_1 .
- Hypothetical poles are not active in the range of low frequencies that will be considered in our traffic flow modeling applications.

3) *Bode plots for congested regime:* We use the same fundamental diagram as in the free-flow case. However the linearization point, $\rho^* = 0.08$ veh/m, corresponds to the congested region of the Greeshields diagram. We show the distributed Bode plots for the



Spatial magnitude Bode plot for $\gamma_{11}(x, s)$.

Fig. 5. Spatial magnitude Bode plots for Riemann invariants in congested regime ($|\alpha| = 0.05$ Hz)

Riemann invariants in Figure 5 and for the physical variables in Figure . In that case, $\alpha = 0.05$ Hz, which does correspond to a reasonable characteristic frequency for traffic modeling applications.

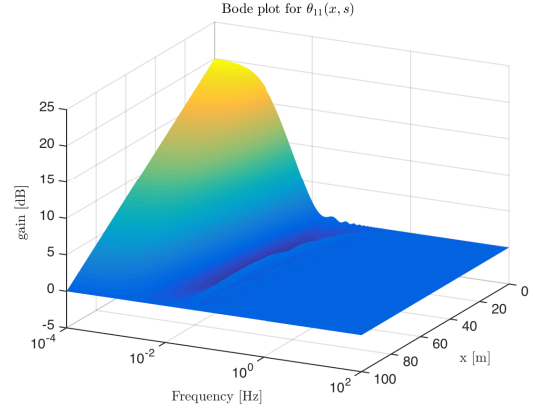
Similarly to the free-flow case, for high frequencies ($w \gg 2\pi \frac{\lambda_1 \tau \alpha}{L} = 0.13$ Hz) near zero values appearing with spatial periodicity $\frac{2\pi}{w} \lambda_1 \tau \alpha$ almost cancel out γ_{21} , θ_{12} , and θ_{21} . Such points only appear as irregularities in the Bode plots because the gain is computed on a logarithmic scale.

4) *Poles and BIBO stability of the system:* In order to practically assess the presence of poles, numerical search for roots of the denominator of the transfer functions has been conducted thanks to standard equation solvers. Once more $-\alpha$ is a solution and another one was found at $s = -0.0018$. They are both negative reals and therefore cannot make the system unstable. Although the solvers could have detected poles with a non zero imaginary part, none has been found. Holistic search for other poles should be conducted but is out of the scope of this article.

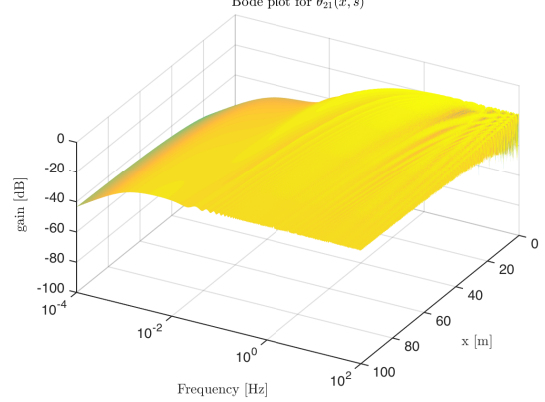
D. Findings and conclusion from the theoretical study

The numerical experiments above have validated the accuracy of the linearized model and highlighted several of its core properties.

- The TFN delineates two regimes: congested for $F > 1$ and free-flowing for $F < 1$. This classification, and the resulting stability result legitimize the use of linearization about a nominal point in the stable region.
- The assessment of convective instability in the free flow regime is of course applicable to this specific model (other models such as [?] might lead to other conclusions, and all need to be checked against experimental data). Here, exponential growth of the linearization error only occurs in a conic region of the $[0, T] \times [0, L]$



Spatial magnitude Bode plot for $\theta_{11}(x, s)$.



Spatial magnitude Bode plot for $\theta_{21}(x, s)$.

Fig. 6. Spatial magnitude Bode plots for physical variables in congested regime ($|\alpha| = 0.05$ Hz)

domain where convective instability travels along the characteristics.

- The absolute value of the term $\alpha = -\frac{\lambda_2}{\tau(\lambda_1 - \lambda_2)}$ is a characteristic frequency of the system. It delineates the low frequency domain in which approximate expressions help decompose the transfer functions in simple gain and delay components. In the spectral domain, λ_1 and λ_2 appear as information propagation speeds in distributed delay elements while $\tau \lambda_1$ acts as the characteristic distance of distributed gain components.

IV. NUMERICAL VALIDATION

In this section we demonstrate the ability of the linearized ARZ equations to model the various non-linear dynamics around a nominal operation point. The spectral form of the linearized model provides a well-established control theoretic framework for designing control strategies for the system. Prior to using such techniques, it is necessary to assess how accurate the model is in its linearized form. This section compares the prediction of the model with actual flow and velocity data gathered from the well-known NGSIM

data set.

A. Data source: NGSIM trajectories

We use the NGSIM trajectory data set for a section of the US-101 highway. The set gathers trajectories of vehicles sampled with a 10 Hz frequency thanks to high precision cameras. The data is pre-processed so as to take only cars into account; 45 minutes are recorded on a 650-meter long section with five lanes. The lanes are taken into account when computing the lineic density of vehicles ρ . A map of the time evolution of speed along the section is given in Figure 7. Only a subset of the spatial domain is used due to the presence of ramps, which breaks the homogeneity of the freeway. The viable domain is 200 meters long.

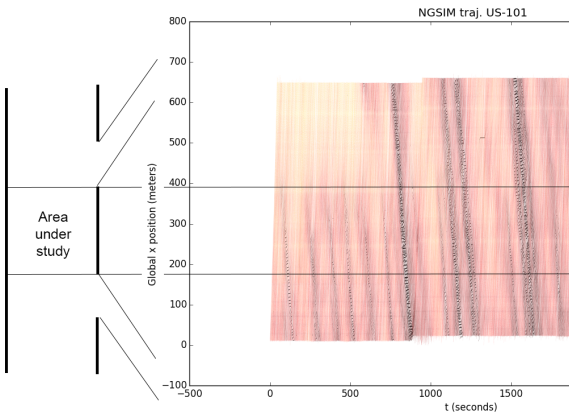


Fig. 7. NGSIM trajectories. Color represents the measured speed of each car in m/s.

B. Reconstructing (v, q) maps from NGSIM trajectories

The NGSIM data set does not directly provide the values $v(t, x)$ and $q(t, x)$ in the resolution domain $[0, T] \times [0, L]$. To obtain macroscopic quantities out of the microscopic measurements, we follow the approach devised in [?] and divide the space-time grid into cells $([i\Delta t, (i+1)\Delta t] \times [j\Delta x, (j+1)\Delta x])_{i \in \{1 \dots n_t\}, j \in \{1 \dots n_x\}}$, where n_t and n_x are the number of cells in time and space, respectively. We denote each cell as $\text{bin}_{i,j}$. This operation consists of gathering corresponding data points into cells, then estimating the quantities of interest in each cell, it was for example used in [?].

Within each cell, a specific number of traces, or footprints of a vehicle along its trajectory, are available, and ρ , v , and q are assumed to be constant. We present several formulae to map a set of traces to speed, flow, and density over the space-time grid.

Binning formula for v : Since the speed is assumed to be constant in each cell, a straightforward estimate

for the speed is the empirical average. The estimator for v in $\text{bin}_{i,j}$ is

$$\hat{v}_{i,j} = \text{mean}_{\text{trace} \in \text{bin}_{i,j}}(v(\text{trace})). \quad (51)$$

Binning formula for ρ : By definition, the density of $\text{bin}_{i,j}$ is

$$\rho_{i,j} = \frac{1}{n_{\text{lanes}} \Delta x \Delta t} \iint_{(t,x) \in [i\Delta t, (i+1)\Delta t] \times [j\Delta x, (j+1)\Delta x]} \rho(x, t) dx dt. \quad (52)$$

The position of each vehicle is recorded every 0.1 second. For each cell we count the number of traces and normalize it by the sampling rate. The contribution of a given vehicle to the density of a cell is proportional to the number of traces it has left in the cell. If the speed is assumed to be locally constant, this contribution is proportional to the time this vehicle spends in the cell and is consistent with the conservation of the total number of vehicles across all cells. Then we have the density estimator

$$\hat{\rho}_{i,j} = \frac{\text{card}(\{\text{trace} \mid \text{trace} \in \text{bin}\})}{n_{\text{lanes}} \Delta x \Delta t \text{ sampling rate}} \quad (53)$$

where $\text{card}(\cdot)$ gives the number of elements in a set, i.e., its cardinal.

Binning formula for q : By definition, $q = \rho v$, so a logical first estimate for q in $\text{bin}_{i,j}$ is

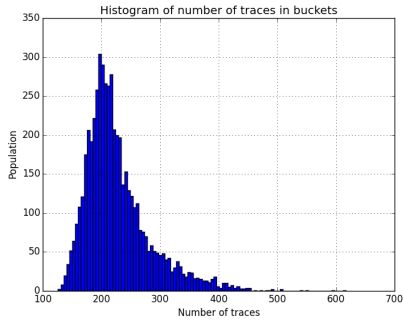
$$\hat{q}_{i,j}^1 = \hat{v}_{i,j} \hat{\rho}_{i,j}. \quad (54)$$

We can also approximate the flux through $\text{bin}_{i,j}$ with a simple counting method. If a vehicle crosses spatial coordinate $(j+1)\Delta x$ between times $i\Delta t$ and $(i+1)\Delta t$, then it leaves a trace in both $\text{bin}_{i,j}$ and $\text{bin}_{i,j+1}$. Counting these vehicles and normalizing by the duration Δt gives the estimator

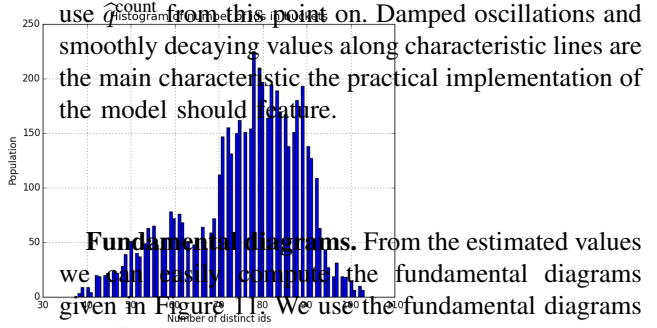
$$\hat{q}_{i,j}^{\text{count}} = \frac{1}{n_{\text{lanes}} \Delta t} \text{card}(\{\text{id}(\text{trace}) \mid \text{trace} \in \text{bin}_{i,j}\} \cap \{\text{id}(\text{trace}) \mid \text{trace} \in \text{bin}_{i,j+1}\}) \quad (55)$$

where $\text{id}(\cdot)$ gives the identification number of a vehicle.

1) Choosing the number of bins: As the estimation formulae above rely on averaging, having a comfortable number of points in each bin provides more stable estimates. It is worth mentioning that usual central limit theorem based reasoning for convergence of such estimates is flawed as several samples may correspond to the same vehicle or interacting vehicles, violating the independence assumption of the theorem. Proving the convergence of the estimates above lies beyond the scope of this article. As a rule of thumb we choose a discretization that guarantees that most bins will host more than 100 traces. This is achieved with a 80×80 grid where the 10th percentile of the number of traces in a given bin is 170. Such a grid also yields a 10th percentile of 56 distinct vehicles per bin. The histograms of number of traces and vehicle per cell are given in Figure 8.



Histogram of number of traces per cell.



use $\hat{q}_{i,j}^{\text{count}}$ from this point on. Damped oscillations and smoothly decaying values along characteristic lines are the main characteristic the practical implementation of the model should feature.

Fundamental diagrams. From the estimated values we can easily compute the fundamental diagrams given in Figure 11¹⁰. We use the fundamental diagrams to calibrate the model parameters. Though the dataset of number of distinct vehicles per cell used is dense, it covers only a small region of time and space. Thus, its small size is a potential flaw in our model parameter calibration as it is certain that our measurements are highly correlated. This seems to be confirmed by the fact that the fundamental diagrams below correspond only to the congested regime.

Fig. 8. Experimental justification for a 80×80 cell based discretization grid for the NGSIM data.

While our goal here is not to present theoretical proofs of the convergence of the binned estimators for (v, ρ, q) , it is nonetheless possible to check that the procedure is coherent. Two estimators are provided for q that use radically different techniques: the first relies on the average measured speed and the number of traces in a bin, while the other relies on counting vehicles transiting from a cell to another. Figure 9 show that the scatter plot of $\hat{q}_{i,j}^{\text{count}}$ plotted against $\hat{q}_{i,j}$ coincides nicely with the line $y = x$, validating the overall binning and estimation procedure above.

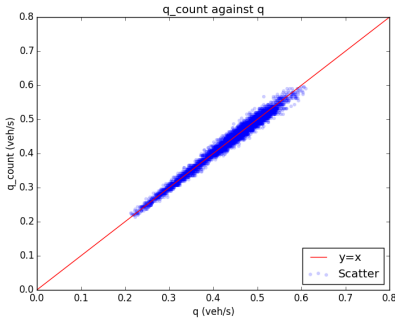
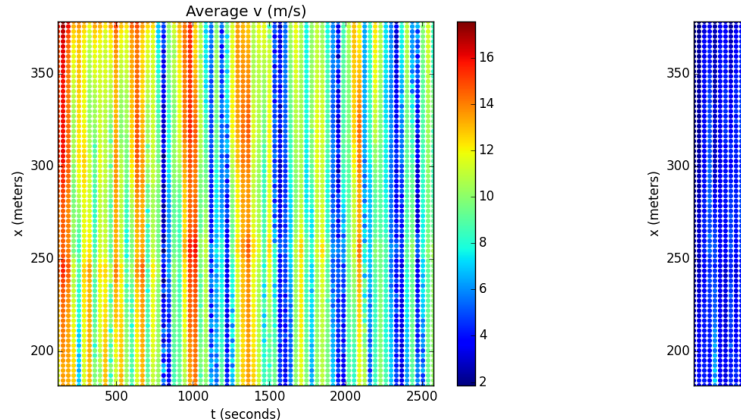


Fig. 9. Sanity check for the estimation procedure. $\hat{q}_{i,j}^{\text{count}}$ is plotted against $\hat{q}_{i,j}$ across the grid of bins.



C. Estimated values for (v, q)

To check how well the linearized ARZ model fits an actual dataset, we chose a bounded domain and compare the theoretical solution given by the second-order model and the observed data. Again we focus on the variables v and q . Using the estimation procedure above, we compute fundamental diagrams from which we estimate the eigenvalues λ_1 and λ_2 . To calibrate the relaxation time τ , we analyze the errors of predicted values of v and q for various τ . The resulting maps of both the predicted and observed values highlight phenomena that the linearized model can and cannot account for.

Maps. The estimates $\hat{v}_{i,j}$, $\hat{\rho}_{i,j}$, $\hat{q}_{i,j}$, and $\hat{q}_{i,j}^{\text{count}}$ are plotted on the discretized grid in Figure 10. Note that \hat{q} and \hat{q}^{count} give extremely similar results, so we may

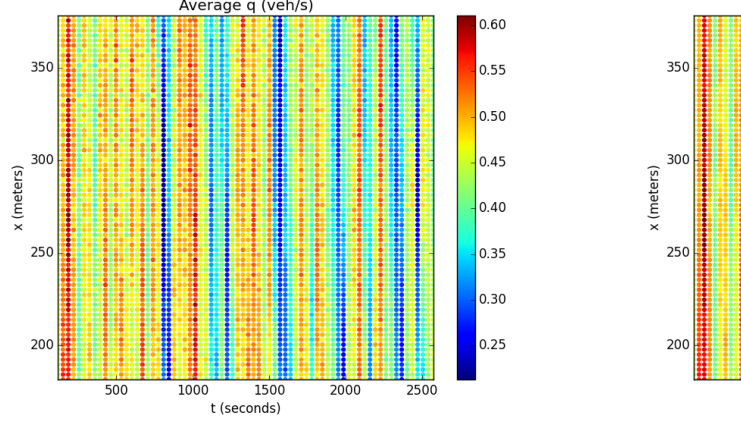


Fig. 10. Estimated values for (v, q, ρ) . Top left: $\hat{v}_{i,j}$. Top right: $\hat{\rho}_{i,j}$. Bottom left: $\hat{q}_{i,j}$. Bottom right: $\hat{q}_{i,j}^{\text{count}}$.

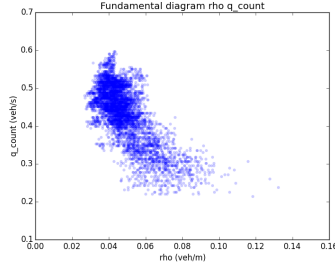


Fig. 11. Empirical fundamental diagrams. Left: $(\hat{\rho}, \hat{q}^{\text{count}})$. Middle: $(\hat{v}, \hat{q}^{\text{count}})$. Right: $(\hat{\rho}, \hat{v})$.

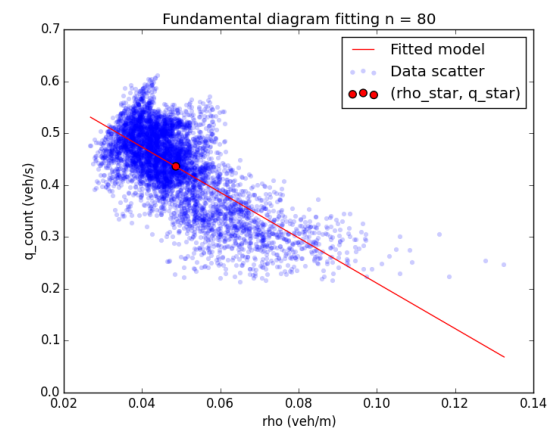


Fig. 12. Calibration of λ_1 and λ_2 . The circle denotes the linearization point. The affine model used to estimate λ_2 and the linearization point is also plotted. The estimates are: $\hat{\lambda}_1 = 8.96$ m/s, $\hat{\lambda}_2 = -4.37$ m/s, $\hat{\rho}^* = 0.049$ veh/m, $\hat{v}^* = 8.96$ m/s, $\hat{q}^* = 0.44$ veh/s, with $r^2 = 0.48$. The characteristic frequency of the system is $\hat{\alpha} = 8.37 \times 10^{-3}$ Hz. Its order of magnitude does correspond to practical traffic flow modeling.

D. Verification of the spectral form

Calibration of λ_1 and λ_2 , linearization point. In Section II, we found that λ_1 is exactly v^* and λ_2 is the slope of the fundamental diagram at v^* . Thus to calibrate the eigenvalues we must find the linearization point. We estimate the linearization point using the Ordinary Least Squares method. Note the dataset used corresponds only to the congested regime and the fundamental diagram is almost affine. The estimator, $\hat{\lambda}_1 = \hat{v}^*$ is chosen as the empirical mean of $\hat{v}_{i,j}$. To estimate λ_2 , we fit a linear model $\hat{q}^{\text{count}} = b_1 \hat{\rho} + b_0 + \epsilon$, where ϵ represents the noise in the model that would ideally be centered, homoschedastic, and uncorrelated but is not practically. Then $\hat{\lambda}_2 = \hat{b}_1$ and we take \hat{q}^* as the empirical average of \hat{q}^{count} . The ratio of \hat{q}^* and \hat{v}^* gives the estimate $\hat{\rho}^*$. Provided each estimator is convergent, the continuity of the functional $(x, y) \rightarrow \frac{x}{y}$ on its domain guarantees the convergence of $\hat{\rho}^*$. The empirical results are presented in Figure 12. The determination coefficient is poor but can be improved by filtering out outliers and gathering more data. Future work should include improving the quality of the estimation. Significance tests for the coefficients of the linear model are not presented. The assumptions they rely on about the linear dependency between \hat{q} and \hat{v} are clearly not respected here as the noise is auto-correlated. Further work should also turn this rather heuristic method for estimating parameters into a fully justified statistical procedure. Note that the goal of the present article is to provide a new model and corresponding spectral analysis, which we want to illustrate with state of the art data. Thus, development of statistical methods to handle this data is out of the scope of the present investigation.

In this section we demonstrate the performance of the spectral form as a prediction tool using the time domain responses derived from the transfer functions (see ??) and FFT. Since we are working with a linearized system, we can decompose boundary conditions then add predicted values inside the domain $[0, T] \times [0, L]$. Fourier decomposition of boundary conditions is here extremely accurate as the median relative errors for the interpolation of the values of $\xi_1(x = 0, \cdot)$ and $\xi_2(x = L, \cdot)$ are respectively 2% and 3%.

Simulated maps. Since the spectral form presents information in the diagonalized basis, we need a conversion before we can compare the simulated results to the values estimated from the dataset. To make a comparison in the diagonalized basis, we first compute the estimated deviations from the equilibrium $\hat{\tilde{v}}_{i,j} = \hat{v}_{i,j} - \hat{v}^*$ and $\hat{\tilde{q}}_{i,j} = \hat{q}_{i,j} - \hat{q}^*$. Then the estimates for ξ_1 and ξ_2 are given by $\hat{\xi}_{1,i,j} = \frac{\hat{\rho}^* \hat{\lambda}_2}{\hat{\lambda}_1 - \hat{\lambda}_2} \hat{\tilde{v}}_{i,j} + \hat{\tilde{q}}_{i,j}$ and $\hat{\xi}_{2,i,j} = \frac{\hat{\rho}^* \hat{\lambda}_1}{\hat{\lambda}_1 - \hat{\lambda}_2} \hat{\tilde{v}}_{i,j}$. To compare the physical variables, we compute the velocity and flow predictions by inverting (31): $\tilde{q} = \xi_1 - \frac{\lambda_1}{\lambda_2} \xi_2$, $\tilde{v} = \frac{\lambda_1 - \lambda_2}{\rho^* \lambda_1} \xi_2$.

Figure 13 shows important qualitative properties of the model. As expected, the model generally predicts with very good accuracy the decay of all quantities along their characteristic lines, a realistic feature that cannot be paralleled by first-order models. The general quality of the fit is rather good with most of the error on v and q in a 20% range of the data's amplitude between minimum and maximum values. Furthermore the linearized second-order model manages to capture oscillations observed on the boundary and account for their decay accurately.

Calibration of τ For each τ we compute the *mean absolute error* (MAE), or the average difference in absolute value between simulated and predicted values for each discretization cell. Since the quantities v and q are not physically homogeneous, it is not sensible to aggregate the errors over these quantities. However, ξ_1 and ξ_2 are both expressed in veh/s. Summing their MAE gives a reliable uni-dimensional index of the quality of the fit with respect to τ . This quantity is computed for different values of τ ranging from 5 to 80 seconds. The value offering the best fit is $\tau^* = 39.18$ s.

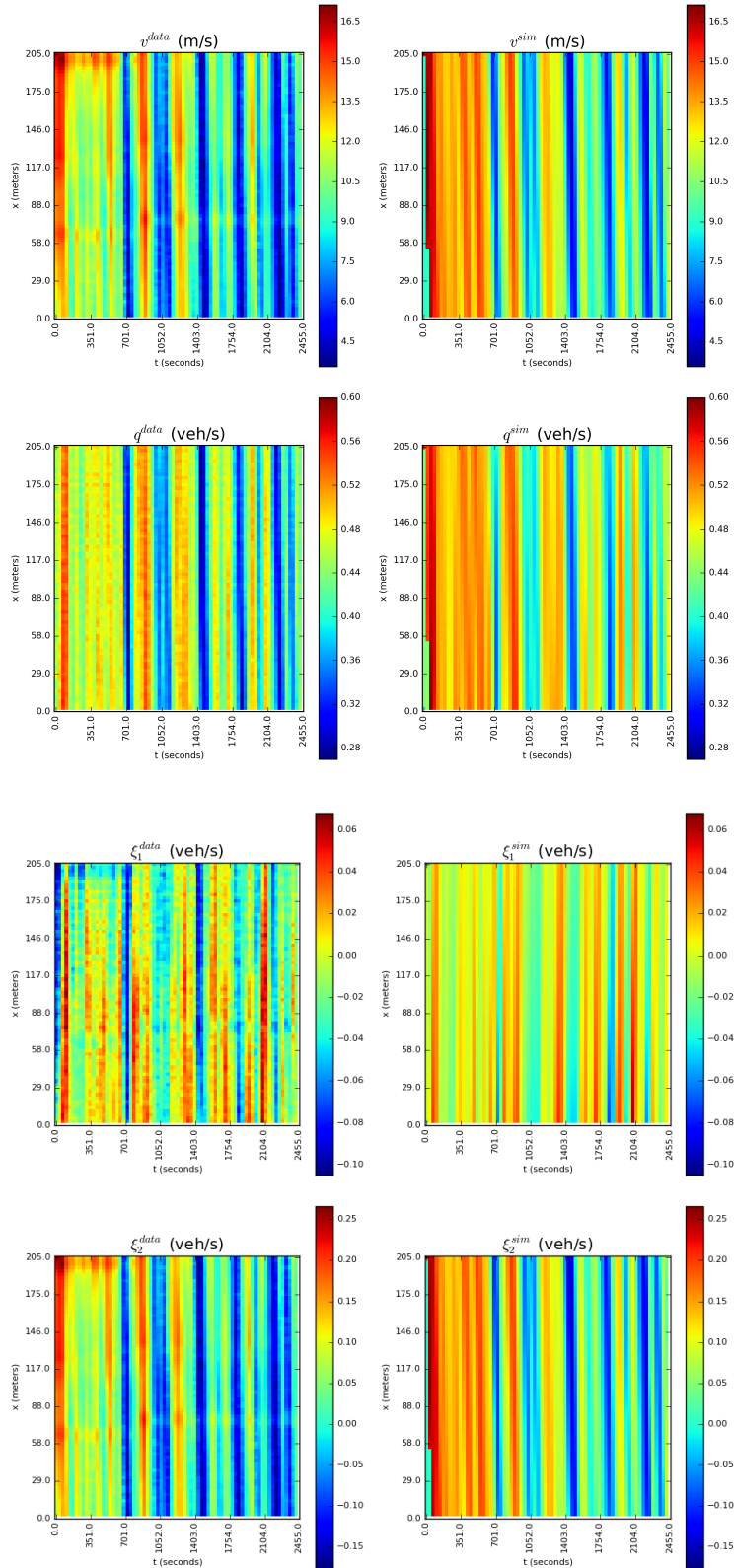


Fig. 13. Data versus predicted. Top Figure: (v, q) domain, top row is v , bottom row is q . Bottom: (ξ_1, ξ_2) domain, top row is ξ_1 , bottom row is ξ_2 . First column: data. Middle column: predictions. Third column: error (difference between prediction and data).

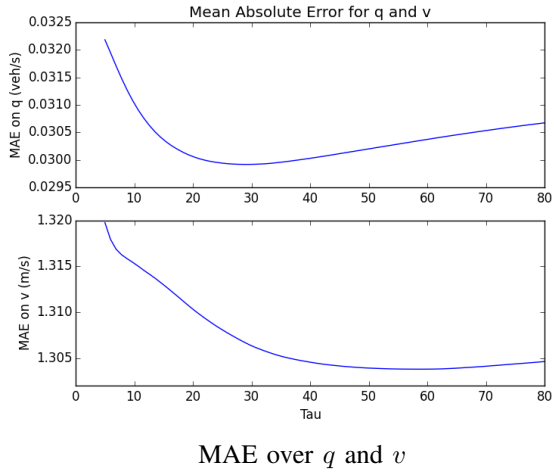


Fig. 14. Calibration of τ , one minimizes the sum of MAE over ξ_1 and ξ_2 .

E. Findings and conclusion from the numerical experiments

The numerical experiments above have validated the accuracy of the linearized model and highlighted several of its core properties.

- The numerical experiments above show that the linearized ARZ model is capable of reproducing NGSIM data accurately for a homogeneous segment of the US-101 freeway. Oscillations are accounted for as well as their damping delay.
- The spectral approach provided here supports a solution to the underlying traffic flow model. In other words, the contribution of the work is to show that the model can support oscillatory behavior (through periodic solutions). This is the main difference with purely data driven approaches such as [?] for example.

V. CONCLUSION

As the full nonlinear ARZ equations have no known closed form solutions in the general case, they are difficult to analyze. The linearized equations enable the use of spectral methods presented here, allowing for elegantly simple yet powerful analysis tools relying on explicit solutions. These equations are diagonalized, and solved explicitly using a spectral representation (distributed transfer function). Using this approximation, we are able to analyze them around a nominal flow and characterize the oscillatory behavior of the solution. The linearized model is able to capture important features of the flow which first order models cannot.

With the linearized ARZ model, we were also able to define the Traffic Froude Number F . This quantity is computed using the eigenvalues of the system and characterizes the flow regime of the road section under consideration.

Considering the transfer function of the linearized system of equations delineates the conditions for sta-

bility of the approximation about the equilibrium. The time domain responses we derive show that the system is unstable when one of the eigenvalues is negative. In the free flow regime, $F < 1$, values of flow and speed increase exponentially in a cone region of space and time and the system leaves the linear regime, while in the congested regime, $F > 1$, oscillations decrease. In the latter case, the system remains in the linear regime and oscillations on boundary conditions are damped with an exponential rate along the characteristic lines. Thus the TFN is also an indicator of linear stability.

The behavior predicted in congested regime for traffic does not present shocks and Fourier spectral analysis cannot account for more nonlinear and non-smooth behavior as well as wavelet transforms. However, our spectral domain study paves the way to applying standard linear system control theory to traffic, with a linearized second model that is empirically reliable in terms of reproducing actual data. Future work will therefore focus on controller design based on the spectral framework presented here.

APPENDIX

The aim is to derive the time domain responses of generic input signals such as $t \rightarrow H(t)$ and $t \rightarrow \cos(\omega t + \phi) H(t)$ when multiplied in the Laplace domain by $\frac{1}{s+\alpha}$. This then enables the computation of any response that decomposes in a Fourier transform.

A. Step function input

The time domain input function is $H(t)$. One computes the inverse Laplace transform of $s \rightarrow \frac{1}{s(s+\alpha)}$ which is

$$t \rightarrow \frac{1}{\alpha} (1 - e^{-\alpha t}) H(t)$$

B. Phased cosine input

The time domain input function is $\cos(\omega t + \phi) H(t)$. One computes the inverse Laplace transform of $s \rightarrow \frac{1}{s+\alpha} \left\{ \frac{s}{s^2+\omega^2} \cos(\phi) - \frac{w}{s^2+\omega^2} \sin(\phi) \right\}$ which can be directly achieved in the time domain. Indeed, the result is given by the convolution product $t \rightarrow (e^{-\alpha t} H(\cdot) * \cos(\omega \cdot + \phi) H(\cdot))(t)$, that is to say

$$t \rightarrow \frac{-e^{-\alpha \cdot t} (\alpha \cdot \cos(\phi) + w \cdot \sin(\phi)) + \alpha \cdot \cos(\omega t + \phi) + w \cdot \sin(\omega t + \phi)}{\alpha^2 + w^2} H(t) = \kappa_{\alpha, w, \phi}^{\cos}(t)$$

C. Fourier sum input

Let the input be $t \rightarrow \mu H(t) + \sum_{k=1}^n \beta_k \cdot \cos(k \cdot \omega t + \phi_k) H(t)$. The time domain response is therefore

$$t \rightarrow \frac{\mu}{\alpha} (1 - e^{-\alpha t}) H(t) + \sum_{k=1}^n \beta_k \cdot \kappa_{\alpha, w, \phi}^{\cos}(t)$$

D. Fourier decomposition and time domain responses for $\lambda_2 > 0$

Let $\alpha = -\frac{\lambda_2}{\tau(\lambda_1 - \lambda_2)} < 0$.

$$\begin{pmatrix} \widehat{\xi}_1(x, s) \\ \widehat{\xi}_2(x, s) \end{pmatrix} = \Phi(x, s) \begin{pmatrix} \widehat{\xi}_1(0, s) \\ \widehat{\xi}_2(0, s) \end{pmatrix}$$

with

$$\Phi(x, s) = \begin{bmatrix} e^{-\frac{sx}{\lambda_1}} e^{-\frac{x}{\lambda_1 \tau}} & 0 \\ -\alpha \frac{\lambda_1}{\lambda_2} \left(e^{-\frac{sx}{\lambda_1}} e^{-\frac{x}{\lambda_1 \tau}} - e^{-\frac{sx}{\lambda_2}} \right) \frac{1}{s+\alpha} & e^{-\frac{sx}{\lambda_2}} \end{bmatrix}$$

implies the following fundamental responses for the system.

1) Fundamental responses in time domain::

- $\begin{pmatrix} \xi_1(0, t) \\ \xi_2(0, t) \end{pmatrix} = \begin{pmatrix} H(t) \\ 0 \end{pmatrix}$:

- $\xi_1(x, t) = e^{-\frac{x}{\lambda_1 \tau}} H\left(t - \frac{x}{\lambda_1}\right)$

- $\xi_2(x, t) = -\frac{\lambda_1}{\lambda_2} \left(e^{-\frac{x}{\lambda_1 \tau}} \left(1 - e^{-\alpha \left(t - \frac{x}{\lambda_1} \right)} \right) H\left(t - \frac{x}{\lambda_1}\right) \right)$

- $\begin{pmatrix} \xi_1(0, t) \\ \xi_2(0, t) \end{pmatrix} = \begin{pmatrix} 0 \\ H(t) \end{pmatrix}$:

- $\xi_1(x, t) = 0$

- $\xi_2(x, t) = H\left(t - \frac{x}{\lambda_2}\right)$

- $\begin{pmatrix} \xi_1(0, t) \\ \xi_2(0, t) \end{pmatrix} = \begin{pmatrix} \cos(\omega t + \phi) \\ 0 \end{pmatrix}$:

- $\xi_1(x, t) = 0$

- $\xi_2(x, t) = \cos\left(\omega\left(t - \frac{x}{\lambda_2}\right) + \phi\right) H\left(t - \frac{x}{\lambda_2}\right)$

E. Fourier decomposition and time domain responses for $\lambda_2 < 0$

This time, $\alpha = -\frac{\lambda_2}{\tau(\lambda_1 - \lambda_2)} > 0$.

$$\begin{pmatrix} \widehat{\xi}_1(x, s) \\ \widehat{\xi}_2(x, s) \end{pmatrix} = \Phi(x, s) \begin{pmatrix} \widehat{\xi}_1(0, s) \\ \widehat{\xi}_2(L, s) \end{pmatrix}$$

$$\Gamma(x, s) = \left(\alpha \frac{\lambda_1}{\lambda_2} \left(e^{-\frac{x}{\lambda_1 \tau}} e^{-\frac{sx}{\lambda_1}} - e^{-\frac{L}{\lambda_1 \tau}} e^{-\frac{s}{\lambda_2} \left(x - L \frac{\lambda_1 - \lambda_2}{\lambda_1} \right)} \right) \frac{1}{s+\alpha} \right) e^{-\frac{sx}{\lambda_2}}$$

implies the following fundamental responses for the system.

I) Fundamental responses in time domain:

- $\begin{pmatrix} \xi_1(0, t) \\ \xi_2(L, t) \end{pmatrix} = \begin{pmatrix} H(t) \\ 0 \end{pmatrix}$:

- $\xi_1(x, t) = e^{-\frac{x}{\lambda_1 \tau}} H\left(t - \frac{x}{\lambda_1}\right)$

- $\xi_2(x, t) = H\left(t - \frac{x-L}{\lambda_2}\right)$

- $\begin{pmatrix} \xi_1(0, t) \\ \xi_2(L, t) \end{pmatrix} = \begin{pmatrix} 0 \\ H(t) \end{pmatrix}$:

- $\xi_1(x, t) = 0$

- $\xi_2(x, t) = H\left(t - \frac{x-L}{\lambda_2}\right)$

- $\begin{pmatrix} \xi_1(0, t) \\ \xi_2(L, t) \end{pmatrix} = \begin{pmatrix} \cos(\omega t + \phi) \\ 0 \end{pmatrix}$:

- $\xi_1(x, t) = e^{-\frac{x}{\lambda_1 \tau}} \cos\left(\omega\left(t - \frac{x}{\lambda_1}\right) + \phi\right) H\left(t - \frac{x}{\lambda_1}\right)$

- $\xi_2(x, t) = -\frac{\lambda_1 \alpha}{\lambda_2} \left(e^{-\frac{x}{\lambda_1 \tau}} \kappa_{\alpha, \omega, \phi}^{\cos}\left(t - \frac{x}{\lambda_1}\right) - e^{-\frac{L}{\lambda_1 \tau}} \kappa_{\alpha, \omega, \phi}^{\cos}\left(t - \frac{x-L}{\lambda_2}\right) \right)$

- $\xi_1(x, t) = 0$

- $\xi_2(x, t) = \cos\left(\omega\left(t - \frac{x-L}{\lambda_2}\right) + \phi\right) H\left(t - \frac{x-L}{\lambda_2}\right)$

ACKNOWLEDGMENTS

The authors wish to thank Dr. Nikolaos Bekiaris-Liberis and Pierre-Olivier Lamare (PhD student at laboratoire Jean Kuntzmann) for their support in the first steps of adapting the spectral method from the Saint-Venant equation framework to the ARZ model. Professor L. Craig Evans' help has been extremely precious in understanding core theoretical properties of the linearized ARZ equations. The authors are also grateful to Dr. Guillaume Costeseque for his insightful comments on the draft.

REFERENCES